From Tropospheric Folding to Khamsin and Foehn Winds: How Atmospheric Dynamics Advanced a Record-Breaking Dust Episode in Crete

Stavros Solomos , Nikos Kalivitis , Nikos Mihalopoulos , Vassilis Amiridis , Giorgos Kouvarakis , Antonis Gkikas , Ioannis Binietoglou , Alexandra Tsekeri , Stelios Kazadzis , Michael Kottas , Yaswant Pradhan , Emmanouil Proestakis , Panagiotis Nastos , Franco Marenco

[1]IAASARS, National Observatory of Athens, Athens, 15236, Greece

[2]Chemistry department, University of Crete, 71003 Heraklion, Crete, Greece

[3]IERSD, National Observatory of Athens, 15236 Athens, Greece

[4]Physikalisch-Meteorologisches Observatorium Davos, World Radiation Center, Dorfstrasse 33, CH-7260 Davos Dorf, Switzerland

[5]Satellite Applications, Met Office, Exeter, UK

[6]Laboratory of Climatology and Atmospheric Environment, National and Kapodistrian University of Athens, Athens, 15784m Greece

[7]National Institute of R & D for Optoelectronics, Magurele, Ilfov, Romania

Abstract A record-breaking dust episode took place in Crete on 22 March 2018. The event was characterized by surface concentrations exceeding 1 mg m^{-3} for a period of 4-7 hours, reaching record values higher than 6 mg m^{-3} at the background station of Finokalia. We present here a detailed analysis of the atmospheric dynamical processes during this period, to identify the main reasons that resulted in such extreme dust advection over Crete. At synoptic scale, the weakening of the polar vortex and the meridional transport of polar air masses at upper tropospheric layers resulted in a strong jet streak over N. Africa and Central Mediterranean and corresponding tropospheric folding that brought cold stratospheric air in mid and upper troposphere. Cyclogenesis occurred at the Gulf of Sirte in Libya, resulting on strong winds over the NE parts of Libya, enhancing particle emissions. The dust plume traveled at low heights (0.5-3 km) along the warm conveyor belt preceding the depression cold front. This type of dusty southerly wind is commonly known as “Khamsin”. As the flow approached Crete, Foehn winds at the lee side of the island favored the downward mixing of dust towards the surface, resulting in local maxima of PM_{10} in Heraklion and Finokalia. The analysis is based on the synergy of high resolution WRF-Chem simulations reaching up to 1×1 km grid space over Crete, ground-based and satellite remote sensing of the dust plumes (PollyXT lidar, MSG-SEVIRI, MODIS) and detailed surface aerosol in-situ measurements at urban (Heraklion, Chania) and background (Finokalia) stations in Crete.

Keywords: dust; polar vortex; Khamsin; Foehn; cyclogenesis; tropospheric folding; Finokalia

Introduction

Mineral dust particles that are emitted from the desert areas in Sahara and the Middle East travel long distances in the atmosphere and affect air quality, weather, climate and local ecosystems at the Mediterranean basin (Gerasopoulos et al., 2006; Balis et al., 2006; Kalivitis et al., 2007; Amiridis et al., 2009). Dust affects the radiative transfer in the area (Kushta et al., 2014; Gkikas et al., 2017; Kosmopoulos et al., 2017), and also cloud processes due to the activation of dust particles as cloud condensation nuclei (CCN) and ice nuclei (IN) (Solomos et al., 2011, Kallos et al., 2014). Moreover, the ocean depositions of dust affect biogeochemical processes and phytoplankton blooming (Jickells et al., 2005; Okin et al., 2008). In terms of health impacts, increased PM_{10} concentrations of fine dust aerosols may cause transpiratory diseases and other related health issues (Derbyshire, 2007; Mitsakou et al., 2008; Nastos et al., 2010; Samoli et al., 2011). The island of Crete is very often affected by windblown dust originating from Sahara, due to its proximity to the Africa coastline. In terms of health effects, the severity of the dust events is mainly dictated by the amounts of dust aerosol near the surface. Such conditions with increased surface PM_{10} of Saharan origin are more often found in Crete when the air masses originate from the nearby dust sources of Libya (Nastos, 2012).

In general, the most crucial parameter for the activation of dust emissions is the near surface wind. Such increased wind speeds may occur due to synoptic wind forcing, due to topographic effects (e.g. valley channeling), due to low level jets (LLJ) (Schepanski et al., 2015) or due to squall lines and storm downdrafts (e.g. Solomos et al., 2012, 2017). However, most of the above processes result in detached elevated dust plumes over the Mediterranean. For example, most dust layers in the area are observed at heights 4-5 km in the troposphere and are associated either with Mediterranean low pressure systems or with the summer anticyclonic circulation over N. Africa (Papayiannis et al., 2008; Gkikas et al., 2015; Marinou et al., 2017). In order for the surface PM_{10} concentration in Crete to increase at significant levels, the mesoscale circulation needs to favor transport directly from the coastal dust sources of Libya towards Crete. This type of flow is commonly known as “Khamsin” winds in Libya and Egypt and is mostly prominent during spring months (Edgell, 2009). Such conditions result in the generation of dense and low dust clouds that travel inside the lower troposphere and reach the south parts of Crete in less than 12 hours after emission. In such cases Crete’s mountain range acts as a perpendicular barrier to the southern air masses arriving from Libya and Foehn katabatic winds may develop on the lee side of the island causing a significant downward flux. This combination can significantly increase both the temperature and the amounts of dust aerosol at the surface and at the same time decrease the relative humidity with significant implications for human health (Nastos et al., 2011, 2017). Further, the blow of hot and dry Foehn katabatic winds exacerbates the bioclimatic conditions at the northern coastal urban areas of Crete (such as Heraklion), by means of the thermal indices “Physiological Equivalent Temperature; PET” and “Universal Thermal Climate Index; UTCI” (Bleta et al., 2014).

Such meso-γ weather phenomena are not properly represented in global and limited area atmospheric models mainly due to the poor description of topography at meso-β and meso-α grid increment where

most topographic elements are sub-grid features. Even at a relatively fine grid-space for weather forecasting (e.g. 5-10 km) the actual resolved topography is at a scale of 4Δx (Pielke et al., 2002), implying that the explicit resolving of Foehn winds would require a grid increment of 1×1 km or finer. In this work we investigate the weather processes from synoptic down to meso and local atmospheric scales during a record-breaking dust event that took place in March 2018 in Crete based on synergistic analysis of high resolution modeling, remote sensing and in-situ data. The study is divided in 3 sections. Section 1 includes the description of methodological and analysis tools. In Section 2 we present the main findings regarding the multi-scale atmospheric dynamics and the dust measurements during the event. Section 3 is a summary and discussion of the main findings.

1. Methodology

The methodology consists of synergistic observational and modeling approach, using the resources of the Greek National Research Infrastructure (RI) PANACEA (PANACEA- PANhellenic infrastructure for Atmospheric Composition and climatE change), operating the national facilities of the ACTRIS RI (Aerosols, Clouds, and Trace gases Research Infrastructrure: https://www.actris.eu/).

1.1 Modeling

We use the limited area model WRF-Chem in a two-way nesting configuration in order to describe the physical processes at various atmospheric scales. The grid-space for the external domain is set at 12×12 km. An intermediate domain at 3×3 km is used over Crete and the surrounding region and the inner grid is set at 1×1 km covering the entire island of Crete. This domain structure is shown in Figure 2c. An additional sensitivity run is also performed with a 24×24 km domain covering the same region as the 12×12 km domain. We initialize the main run at 21 March 2018, 00:00 UTC and run it until 23 March 12:00 UTC (T+60). The internal 3×3 km and 1×1 km domains are activated for the period 21 March 18:00 UTC – 22 March 18:00 UTC and 22 March 12:00-18:00 UTC respectively. The model is driven by initial and boundary conditions from the NCEP final analysis (FNL) dataset at 1°×1° grid space and the sea surface temperature is also the NCEP SST at 1°×1°. The planetary boundary layer scheme is the Mellor-Yamada-Janjic and the land properties are parameterized by the Noah Land Surface Model (Chen and Dudhia, 2001a, 2001b). Radiative transfer is computed by the Rapid Radiative Transfer Model (Iacono et al., 2008) for both short-wave and long-wave radiation taking also into account the effects of dust particles in radiative transfer.

The emission of dust is computed with the Air Force Weather Agency (AFWA) scheme (Jones et al., 2012; Su and Fung, 2015) that is basically following Marticorena and Bergametti 1995 (MB95) for the computation of vertical dust fluxes based on wind friction velocity, soil type and surface moisture. The MB95 dust emission scheme has been widely used and evaluated in global and limited area dust models (e.g. DEAD: Zender 2003; GEOS-Chem: Fairlie et al., 2007; SKIRON: Spyrou et al., 2010, 2018; RAMS: Solomos et al., 2011, 2012, 2017). WRF-Chem includes five dust size bins with effective radii of 0.73, 1.4, 2.4, 4.5 and 8 μm. The modeled dust Aerosol Optical Depth (AOD) at 550 nm (τ_{550}) is calculated using the corresponding column mass load of dust (M) and the extinction efficiencies at 550 nm (Q_{ext550}) of the five WRF sub-bins, as in Eq. 1:

Preprints (www.preprints.org) | NOT PEER-REVIEWED | Posted: 23 May 2018 doi:10.20944/preprints201805.0321.v1

Peer-reviewed version available at Atmosphere 2018, 9, 240; doi:10.3390/atmos9070240

$$\tau_{550} = \sum_{1}^{5} \frac{3}{4\rho_n r_{eff_n}} M_n Q_{ext550_n} \qquad Eq.1$$

Where ρ is the particle mass density, r_{eff} is the effective radius and n denotes the corresponding WRF sub-bin. The extinction efficiencies at 550 nm (Table 1) are calculated with Mie theory (Mie, 1908; Bohren and Huffman, 1983), using a refractive index of 1.55+i0.005 for dust (Kandler et al., 2007). We consider lognormal size distributions for the sub-bins with minimum-maximum radius, effective radius and geometric standard deviations as shown in Table 1. Gravitational settling and surface deposition of dust is based on the parameterization of Wesely, 1989. Wet deposition of dust is not parameterized in these simulations, however it is not considered important since there was no significant rainfall along the major transport path. We performed a 3 day spin up run that is considered sufficient for establishing a regional dust background and for providing the initial dust conditions for the subsequent simulations, taking also into account that the main dust event has a relatively limited geographical and temporal extend.

Table 1. Extinction efficiencies at 550 nm (Q_{ext550}) for the dust sub-bins of WRF-CHEM. The sub-bin characteristics are also provided, in terms of the minimum (r_{min}) and maximum (r_{max}) radius, the effective radius (r_{eff}) and the geometric standard deviation (σ_g) of the sub-bin lognormal size distributions.

$r_{min} - r_{max}$ (μm)	r_{eff} (μm)	σ_g	ρ (kg m^{-3})	Q_{ext550}
0 – 0.1	0.73	2	2500	2.79851
1.0 – 1.8	1.4	2	2650	2.26168
1.8 – 3.0	2.4	2	2650	2.24124
3.6 – 6.0	4.5	2	2650	2.14511
6.0 – 10.0	8.0	2	2650	2.09845

1.2 Remote Sensing

1.2.1 PollyXT lidar

The PollyXT lidar (Engelmann et al., 2016) is located in Finokalia (35°20'15.4"N, 25°40'09.8"E, 238m ASL) and is equipped with three elastic channels at 355, 532 and 1064nm, two rotational-vibrational Raman channels at 387nm and 607nm, two linear depolarization channels at 355nm and 532nm, and one water vapor channel at 407nm. The combined use of its near field and far field telescopes provides reliable vertical profiles of aerosol optical properties from 0.25 to 10km in height.

1.2.2 MSG-SEVIRI - Dust RGB

The Dust RGB implements the information provided by the SEVIRI window channels (at 12, 10.8 and 8.7 μm). The 12 μm and 10.8 μm channels are able to discriminate between land surface temperatures and cloud temperatures. The addition of 8.7 μm channel provides information about trace gases and aerosols. The values assigned to the Red, Green and Blue components for generating Dust RGB composite images are given in Table 2. Each of the components is scaled using the following equation:

Preprints (www.preprints.org) | NOT PEER-REVIEWED | Posted: 23 May 2018 doi:10.20944/preprints201805.0321.v1

Peer-reviewed version available at Atmosphere 2018, 9, 240; doi:10.3390/atmos9070240

$$C_i^{scaled} = \min(X) + \delta X \times \left(\frac{C_i - \min(C_i)}{\delta C_i}\right)^{\frac{1}{\gamma_i}}$$

Where, C_i is the value for red, green and blue components; $\delta C_i = \max(C_i) - \min(C_i)$ for each component; $X = [4, 254]$ is the colour range; $\delta X = \max(X) - \min(X)$ is the number of colours; and γ_i is the respective gamma factor.

Dust RGBs have been successfully used to monitor dust and volcanic ash plumes over land and sea both during day and night. The infrared channels used in the RGB composites are sensitive to various surface and atmospheric properties – the Red and the Blue components in this case determine the presence of dust (i.e., warm with large negative BT difference between 10.8 and 12 micron channels) and therefore depicted as bright magenta (during day) or purple (during night) colour over land. A dusty atmosphere can also be tracked over water as a magenta colour.

Table 2: Dust RGB channel enhancement. The "night-mode" flag is raised when solar zenith angle exceeds 85°

Component	Scaling range	Gama factor
Red	$\begin{cases}1K & (day)\\ 2K & (night)\end{cases} < (BT_{12} - BT_{10.8}) > -4K$	1.0
Green	$\begin{cases}15K & (day)\\ 9K & (night)\end{cases} < (BT_{10.8} - BT_{8.7}) > 0K$	$\begin{cases}3 & (day)\\ 2.25 & (night)\end{cases}$
Blue	$\begin{cases}289K & (day)\\ 293K & (night)\end{cases} < BT_{10.8} > \begin{cases}261K & (day)\\ 243K & (night)\end{cases}$	1.0

1.2.3 MODIS

Columnar AOD observations are obtained from the MODerate resolution Imaging Spectroradiometer on-board the NASA's polar satellites Terra and Aqua since 2000 and 2002, respectively (Remer et al., 2005) (https://ladsweb.modaps.eosdis.nasa.gov/). In the present analysis we use the Level 2 (L2) data of the aerosol optical depth at 550 nm (AOD_{550nm}), acquired from the latest version (Collection 6.1, C061) of the MODIS retrieval algorithm, corresponding to satellite overpasses (swaths) of five minutes time interval and their nominal spatial resolution is 10 km × 10 km at nadir. For our purposes, we have used the "combined" AOD produced via the implementation of the Dark Target (DT) algorithm applied based on different assumptions over maritime areas (Tanré et al., 1997; Levy et al., 2013) and vegetated land (Kaufman et al., 1997, Levy et al., 2013) while above bright surfaces (i.e. deserts) the Deep Blue (DB) approach is followed (Hsu et al., 2004; 2013). The merging procedure of the DT-Land, DT-Ocean and DB AOD products is described in Sayer et al. (2014). Global evaluation studies have shown that the uncertainty of MODIS AOD is lower above sea ± (0.03 + 0.05*AOD_{550}) (Remer et al., 2008) and higher over land ± (0.05 + 0.15*AOD_{550}) (Levy et al., 2010; 2013) while over arid regions, an absolute uncertainty of approximately (0.086+0.56*AOD_{550})/AMF, where AMF is the geometric air mass factor, has been reported by Sayer et al. (2013).

1.3 In-situ measurements

Measurements were performed on the island of Crete at the environmental research station of the University of Crete at Finokalia (35°20'N, 25°40'E). Finokalia environmental research station was established in 1993 and it has been characterized as representative of the background regional conditions for the eastern Mediterranean basin (Lelieveld et al., 2002). PM_{10} concentrations exceedances of the EU limit value of 50 μg m^{-3} (Directive 2008/50/EU) at the station can be attributed entirely to dust transport when the air mas back trajectories originate from northern Africa (Kalivitis et al., 2007). Such events have taken place for ca. 5% of the days since 2004. Additional measurements were available at the atmospheric quality measurement station of the Region of Crete at the cities of Heraklion (35°19'N, 25°7'E) and Chania (32°5'N, 20°16'E). The locations of the three in-situ stations are shown in Figure 8a. The PM_{10} measurements were performed with two identical Thermo ESM Andersen FH 62 I-R beta attenuation particulate monitors with a time resolution of 5 min (Gerasopoulos et al., 2006). Both instruments have been compared to gravimetric techniques in the past with good results (Koulouri et al., 2008).

2. Results

From 1993 to March 2018, the maximum surface concentration of PM_{10} ever observed at Finokalia was 2793 μgm^{-3} (recorded on 24 February 2006 with a time step of 5min). Between 2004 and 2017, only six days with 5 min PM_{10} concentrations larger than 1 mg m^{-3} have been recorded. The Aerosol Optical Depth (AOD) measurements in Crete using the AERosol Robotic network (AERONET) observations (Holben et al., 1998) since 2003, show mean AOD_{500nm} values of 0.19±0.10 with maximum values during April and May (0.24) and mean plus 2 sigma AOD_{500nm} distributions reaching 0.54. For the particular months the minimum Angstrom exponents are observed, with averaged value equal to 0.86.

On March 22, Crete was affected by a particularly severe phenomenon of desert dust transport from northern Africa. This event is seen in the daily composites of MODIS visible channel (Figure 1a,b) and also in the geostationary Dust RGB images of MSG-SEVIRI by the dark magenta region between Africa coast and Crete at 12:00 UTC and 15:00 UTC 22 March 2018 (Figure 1c,d). The presence of dust was initially detected in the western parts of the island (Chania), where the phenomenon peaked at noon, with maximum recorded PM_{10} of 0.5 mg m^{-3}. Meanwhile, in the central and eastern areas (Heraklion and Finokalia) the dust concentrations also begun to increase during the morning hours of 22 March 2018 and in contrast to Chania the dust concentration rather than declining, suddenly began to increase rapidly so that at 15:00 UTC in the afternoon it reached a record value of 4730 μg m^{-3} in Heraklion. The concentration of dust at the easternmost station (Finokalia), increased sharply in the afternoon, and at 17:20 UTC a new record value for Greece was again recorded at 6340 μg m^{-3}, exceeding the 5000 μg m^{-3} upper limit of the tested range reported by the instrument's manufacturer. The average daily values recorded at Chania, Heraklion and Finokalia were 206, 1125 and 850 μg m^{-3} respectively.

2.1 Atmospheric dynamics

In order to understand the main mechanisms leading to this unusual event, we examine the major atmospheric processes taking place in the area starting from synoptic scale dynamics and moving to mesoscale and local dynamics as resolved by WRF-Chem model. At first, the weakening of the arctic polar vortex allows the meridional transport of cold polar air towards Europe on 21 March 2018. This process is evident by the FNL reanalysis of 300 hPa temperature in Figure 2a, where a streak of very low temperatures (lower than -50 °C) is spread throughout Europe and the polar air masses reach south latitudes down to the West Mediterranean at 12:00 UTC, 21 March 2018. WRF-Chem fields from the outer 12×12 km grid are used in the following sections to analyze the impacts of this intrusion in atmospheric circulation. The associated accelerating 300 hPa jet streak is shown in Figure 2b for the next day (at 06:00 UTC, 22 March 2018) presenting a core of maximum wind speeds greater than 70 ms^{-1}. The left exit region of the jet streak is found over the Gulf of Sirte and Central Mediterranean, denoting upper level divergence at this area. Tropospheric folding and the intrusion of stratospheric air at Mediterranean and North Africa latitudes is clearly shown in Figures 2c,d. In Figure 2c the stratospheric air mass is spread southwestwards along the isentropic (iso-theta) surface of 315 K characterized by potential vorticity (PV) up to 10 PVU (1PVU= 10^{-6} m^2 s^{-1} K kg^{-1}). The corresponding potential temperature of this air mass at the height of the dynamical tropopause (iso-2PVU surface) reaches a minimum of less than 300 K over certain parts of the West Mediterranean (Figure 2c). The structure of the eastward propagating trough is shown in Figure 3a at 500 hPa and Figure 3b at 850 hPa on 22 March 06:00 UTC, revealing a negative (northwestward) tilt of the low pressure system with height. The minimum temperatures and geopotential heights at this stage of development are -34 °C, 5400 m and -3 °C, 1340 m at 500hPa and 850 hPa respectively. Moreover, as seen at the 850 hPa map (Figure 3b), a strong baroclinic zone extends from about 20°N, 12°E inside Sahara Desert up to the west coastline of Greece with a horizontal West-East temperature gradient of more than 15 °C between 15°-20° E. This combination of atmospheric dynamics (i.e. tropospheric folding, upper level imbalance, baroclinic trough propagation, lower troposphere baroclinicity) is responsible for the formation and intensification of East Mediterranean cyclones and also for the generation of dust storms (Kaplan et al., 2013; Kouroutzoglou et al., 2015; Pytharoulis 2017).

At mesoscale, the location of cyclogenesis is found on 21 March 2018, 18:00 UTC over the east part of the Gulf of Sirte, as seen by the sea level pressure (slp) minimum of 1000 hPa at this area (Figure 4a). Tropospheric folding is also identified in Figure 4 by the eastward propagation of the stratospheric intrusion and the minimum tropopause heights (geopotential at 2PVU iso-surface) over N. Africa and Central Mediterranean. The depression intensifies as it moves northwards towards the Ionian Sea and reaches minimum slp of 990 hPa at the Gulf of Taranto at 12:00 UTC, 22 March 2018 (Figure 4b). The location of the cold front is identified by the abrupt change in wind direction and the temperature gradient along the 15°E meridian in Figure 5a at 06:00 UTC, 22 March 2018. The warm conveyor belt ahead of the cold front is actually the main driving pathway for the mobilization and transport of dust from Libya towards Crete. As seen in Figure 5b, the near surface dust concentration exceeds 15 mg m^{-3} at certain frontal areas and the low level convergence inside the warm sector actually traps the dust particles ahead of the cold front.

247 **2.2. Dust Transport**

248 The low pressure system remains practically stationary on 22 March 2018 and the location of the
249 conveyor belt preceding the cold is forming a high speed pathway that connects Sahara with Crete. The
250 transport path is shown in Figures 6a-d at 09:00, 12:00, 15:00 and 18:00 UTC respectively, on 22 March
251 2018. The dust plume is constrained inside the warm sector of the depression with dustloads up to 20 g
252 m^{-2} inside the core of the system (i.e. Figure 6b). This type of southerly dusty wind is commonly known
253 in Egypt as "Khamsin" and it develops in East Mediterranean depressions during spring. The core of the
254 system affects Crete between 12:00-18:00 UTC, 22 March 2018.

255

256 **2.2.1 Dust concentrations**

257 The severity of the event is depicted by satellite and model results in Figure 7. MODIS-Terra overpass at
258 09:50 UTC captures an area of AOD up to 5, extending from the coast of Libya towards the cloud-
259 covered region north of 34°N (Figure 7a). Although other aerosols may be also present at this area, this
260 should be attributed to dust according also to the visible channel in Figure1. Furthermore, AOD 5 is the
261 maximum value in MODIS classification (Mamouri et al., 2016) implying that greater values could be
262 actually present at the area. The corresponding model AOD map in Figure 7b exhibits a good spatial
263 agreement with MODIS in dust dispersion but the maximum AOD over the sea does not exceed 3.5
264 implying an underestimation of the modeled optical depth with respect to MODIS. This can be
265 attributed to an underestimation of dust emissions or to latency in dust transport, since the inland
266 model values also exceed 5 and furthermore during the following hours the modeled AOD over the sea
267 also exceeds 6 (not shown).

268 As the plume approaches Crete the flow is deflected eastwards and only parts of the core plume are
269 dispersed over the central and east parts of the island. Surface concentrations in the model exceed
270 6000 μg m^{-3} especially towards the east parts of Crete and near Finokalia station (Figure 8). As seen in
271 Figure 8d the maximum concentrations are found at the leeward side of the highest mountain ridges in
272 Crete, suggesting a downward mixing mechanism i.e. Foehn katabatic winds at these areas. This
273 hypothesis is confirmed by the vertical model cross sections over Finokalia in Figure 9. The presence of a
274 Foehn mechanism is identified in Figure 9a by the descending of the isentropes at the lee side of the
275 mountain range. The downward mixing of the dusty layers increases near surface aerosol concentrations
276 up to 6000 μg m^{-3} and a hydraulic jump is also evident between 35.4° - 35.5° N where the dusty flow
277 bounces back to 2 km height. The katabatic wind speeds reach up to 30 m s^{-1} near the surface and the
278 adiabatic warming of the descending air mass leads to air temperatures exceeding 30 °C at the lee side
279 and to horizontal temperature gradients of more than 10°C between the windward and leeward ridge
280 sides (Figure 9b).

281 **2.2.2 Effects of model grid space on resolved dynamics**

282 This local-scale phenomenon is partially explaining the poor representation of this event in operational
283 dust models. A sensitivity experiment that is shown in Figure 8 clearly displays the effects of resolved

topography in modeled surface dust concentrations. Four different model runs are compared in Figure 8 with identical configuration either than model grid-space. At 24×24 km space (Figure 8a), the model hardly captures Crete topography with a maximum height of 400 m (when the actual highest top is at 2400 m). In this run the dust pattern is literally uninterrupted by the island and the maximum concentration hardly exceeds 2000 μg m^{-3}. At 12×12 km grid space (Figure 8b), the maximum top is at 1000 m, a slight transformation of the flow is evident due to the orographic barrier and an area of maximum dust concentration exceeding 3000 μg m^{-3} appears at the lee side towards the eastern part of Crete. The 3×3 km and 1×1 km runs (Figures 8c,d) both resolve the Foehn mechanism and clearly present maximum concentrations at the lee sides of the mountain ridges (notice also the different topographic contours in these plots). However, the dust concentrations in the finest run are even higher than the 3×3 km run. These results justify the need for high resolution simulations in order to resolve similar events over complex topography, but also raise an interesting consideration on how much more could the model improve by further increasing the grid resolution.

2.2.3 Comparison with observations

In order to examine the spatiotemporal evolution of the extreme dust episode at the station of Finokalia, we analyze the modeled vertical time-height properties of dust concentration, temperature and relative humidity over the station (Figure 10a). The peak of the event is between 16:15 – 17:15 UTC when the modeled surface concentration exceeds 6000 μg m^{-3}. At this time the core of the plume is located at 0.9-1.3 km a.s.l. where dust concentration is higher than 8000 μg m^{-3}. The downward mixing of the dry and warm Saharan air mass is evident in Figure 10 by the abrupt increase in ambient temperature reaching up to 32 °C at 17:00 UTC and by the 10% relative humidity line that actually constraints the katabatic air mass. Comparison of the modeled against measured meteorological values at Finokalia shows that the simulated surface values of temperature and relative humidity are in good agreement and in general following the time-evolution of the in-situ measurements (Figure 10b). An interesting finding arises from the comparison between modeled and measured wind properties. The model reproduces correctly the passage of the cold front. In agreement with the observations the wind is veering from SSE (150°) to WNW (300°) and is also reduced to calm conditions (1.2 m s^{-2}) behind the front (after 17:00 UTC). However, the katabatic Foehn winds are underestimated by almost 10 m s^{-1} at the station location (Figure 10b before 15:00 UTC). This comparison emphasizes on the very local nature of the event and on the large gradients in wind speed induced by the complex topography. For example, values greater than 30 m s^{-1} are only simulated at about 0.5 km above Finokalia station, implying that in reality the station was inside the Saharan layer and even the 1×1 km grid space is not sufficient for accurately reproducing all atmospheric processes near the surface.

Unfortunately, the signal of the PollyXT lidar is most probably attenuated during the specific event. A time window with reliable lidar profiles is only found at 03:00 and 04:00 UTC (Figure 11a). This timeframe corresponds to a different air mass, also carrying Saharan dust that arrives at layers 1.5-6 km over the station. The Klett-Fernald-Sasano method was utilized for the derivation of the extinction coefficient profiles at 532 nm, using a lidar ratio of S=55. The resulting AODs are 2.93 and 1.07 at 03:00 and 04:00 UTC respectively. The dust particle mass concentration profiles of the model (solid line) and PollyXT LiDAR (dashed line) for 03:00 and 04:00 UTC (green and blue line respectively) are also

calculated from these profiles. The dust plume was assumed to be coarse-mode dominated, thus the mass-specific extinction coefficient value of $k_{ext} = 0.52m^2 \cdot g^{-1}$ was utilized for the LiDAR mass concentration profiles (Ansmann, A., et al., 2012). Comparison of modeled dust profiles with these lidar retrievals (Figure 11b) indicates a satisfactory agreement between modeled and observed concentrations in terms of the event scale. The model seems to follow also the modification in maximum concentrations between this 2-hours period. However the depth of the layer is not accurately reproduced especially at 03:00 UTC when the lidar backscatter signal shows a uniform layer of 1000-1600 μg m^{-3} while the modeled profile quickly declines to values less than 1000 μg m^{-3} above 2km. Overall, this comparison may not be representative of the main event, but it generally increases our confidence on the model simulation suggesting also an under-prediction of the actual dust concentrations in the model.

The surface concentrations of PM_{10} in the model are compared with the in-situ measurements at the stations of Finokalia, Heraklion and Chania (Figure 12). The modeled PM_{10} is calculated from the five dust bins as: PM_{10}=bin1+bin2+bin3+0.87·bin4. The local nature of the event is clearly illustrated by the in-situ measurements (dashed lines) in this plot. Finokalia and Heraklion stations, that are located towards the east part of Crete, recorded remarkably increased PM_{10} concentrations exceeding 6 mg m^{-3} during 14:00-18:00 UTC. At the same time, PM_{10} at Chania station that is located 140 km to the west was below 0.2 mg m^{-3}. Taking into account the complexity of the event the model reproduces these record-breaking values in a satisfactory manner, however with several biases. The time evolution of the dust-storm is accurately described and the maximum modeled PM_{10} are also found during 14:00-18:00 UTC in Heraklion and Finokalia. The coevolution of measured and modeled values at these two stations is also evident in Figure 12. The narrow maximum spike of modeled PM10 in Finokalia reaches 5.5 mg m^{-3} one hour earlier than the actual recorded peak of 6.34 mg m^{-3}. However the model clearly underestimates PM_{10} in Heraklion since although the simulation produces very high values exceeding 2.5 mg m^{-3} at this station, the actual concentrations where actually two times higher exceeding 4 mg m^{-3}. In Chania station, the model fails to predict the very low recorded PM_{10} and thus implies a more spatially extended episode than what actually occurred. This is probably explained due to the underprediction of Lefka Ori topography in the model. This mountain range extends south of Chania and acts as a perpendicular barrier to the flow from Africa. It consists of 58 tops exceeding 2 km and even at this high 1×1 km grid space this pattern is not accurately reproduced. As a result, the core of the dust plumes arriving in the model at 1-2 km, instead of being deflected by the mountain range, they actually cross the ridge resulting in katabatic winds at the lee side that affect the west parts of Crete. Actually the coarse 24×24 km model run (Figure 8a) predicts very well the PM_{10} values in Chania but for the wrong reasons. In this run the model hardly sees the Crete Mountains and as a result the dust clouds continue travelling detached towards the north without increasing the surface dust concentration.

3. Summary and Conclusions

We overviewed the most intense Saharan dust episode ever recorded in Finokalia station in Crete during its 14 years operational period (2004-2018). Analysis of the atmospheric processes during this episode suggests that the unique PM_{10} concentrations recorded in Crete on 22 March 2018 were produced by a combination of meteorological processes taking place at various atmospheric scales. In general, the

main driver for strong dust events in Mediterranean is atmospheric dynamics and this particular event is a typical example that combines several of the dynamical processes commonly involved in dust episodes:

- At synoptic scale, the weakening of the polar vortex allows descending of cold stratospheric air of high potential vorticity towards lower latitudes at Mediterranean and N. Africa.
- At mesoscale, the tropospheric folding favors cyclogenesis and intensifies the low pressure systems along the surface baroclinic zones. The formation of mid-latitude cyclones at this area results in mobilization of dust particles from Sahara and the scale and movement of these Mediterranean depressions determines also the dust pathways towards Europe.
- At local scale, the vertical stability of the dusty air mass is disturbed when the plumes reach the orographic barriers of Mediterranean islands (e.g. Crete, Cyprus, Sicily) or the inland continental mountain ranges. Depending on the relevant heights between the mountain ridge and the elevated plumes, topography may act either as a stopping barrier leading in accumulation of dust at the windward ridge (Marinou et al., 2017) or as a primary reason for the generation of katabatic Foehn winds accumulating dust over the leeward side, which was the case for the current event.

From a modeling point of view, resolving of such complex atmospheric patterns is a very challenging task since a high resolution nested grid may be often required at both the origin areas of dust and at the arrival areas, several hundred kilometers away. Our WRF-Chem simulations clearly identify the importance of local scale dynamics on the surface PM_{10}. As expected, the 1×1 km simulation outperforms the coarser 3×3 km, 12×12 km and 24×24 km runs in terms of surface dust concentrations. The major spatiotemporal and quantitative properties of the event are reproduced in satisfactory agreement with the observations, taking into account the complexity of the event. For example the maximum modeled and in-situ PM_{10} in Finokalia is 5.5 mg m^{-3} and 6.34 mg m^{-3} respectively. However, even at the fine grid scale of 1×1km, certain limitations are evident regarding the model performance, mostly related to sub-grid unresolved topographic features and to the associated dynamics induced by terrain variability at the low level tropospheric flow. In general, the event was even more spatially limited than shown in the model and affected only the eastern parts of Crete, leaving the west parts (Chania) practically unaffected.

In this work we explain the physical processes related to atmospheric dynamics during this particular event. Further analysis of the in-situ measurements and of the specific properties of the aerosol particles will follow. Moreover, future work is needed to investigate the impact of climatic forcing to the atmospheric patterns generating such events. Following the consideration that stratospheric intrusions are the primary force for dust-storm generation, any possible future changes in polar vortex properties due to climate change may be relevant to changes in the frequency and strength of dust events in the Mediterranean.

Acknowledgments

The authors acknowledge support from the European Research Council (ERC) Consolidator Grant 2016, D-TECT: Does dust Tribo-electrification affect our Climate? H2020-EU.1.1., Excellent Science, Project ID:

725698; the LIFE Climate Change Adaptation project MEDEA (LIFE16 CCA/CY/000041); and the EU COST Action CA16202 "International Network to Encourage the Use of Monitoring and Forecasting Dust Products (inDust)". The authors gratefully acknowledge Mihalis Lazaridis from the Technical University of Crete for the provision of PM_{10} data for Chania. The authors thank the Group of Atmospheric Optics, Valladolid University, for the provision of the CÆLIS tool (www.caelis.uva.es) used for AERONET data in this publication. Antonis Gkikas acknowledges the DUST-GLASS project funded from the European Union's Horizon 2020 research and Innovation programme under the Marie Skłodowska-Curie grant agreement No 749461. Emmanouil Proestakis and Michael Kottas acknowledge the Stavros Niarchos Foundation for its support.

References

Amiridis, V., Kafatos, M., Perez, C., Kazadzis, S., Gerasopoulos, E., Mamouri, R. E., Papayannis, A., Kokkalis, P., Giannakaki, E., Basart, S., Daglis, I. and Zerefos, C.: The potential of the synergistic use of passive and active remote sensing measurements for the validation of a regional dust model, Ann. Geophys., 27(8), 3155–3164, doi:10.5194/angeo-27-3155-2009, 2009.

Ansmann, A., Seifert, P., Tesche, M. and Wandinger, U.: Profiling of fine and coarse particle mass: case studies of Saharan dust and Eyjafjallajökull/Grimsvötn volcanic plumes, Atmos. Chem. Phys., 12(20), 9399–9415, doi:10.5194/acp-12-9399-2012, 2012.

Balis, D., Amiridis, V., Kazadzis, S., Papayannis, A., Tsaknakis, G., Tzortzakis, S., Kalivitis, N., Vrekoussis, M., Kanakidou, M., Mihalopoulos, N., Chourdakis, G., Nickovic, S., Pérez, C., Baldasano, J. and Drakakis, M.: Optical characteristics of desert dust over the East Mediterranean during summer: a case study, Ann. Geophys., 24(3), 807–821, doi:10.5194/angeo-24-807-2006, 2006.

Bleta, A., Nastos, P. T., Matzarakis, A.: Assessment of bioclimatic conditions on Crete Island, Greece, Reg. Environ. Change, 14, 1967–1981, 10.1007/s10113-013-0530-7, 2014.

Bohren, C. F. and Huffman, D. R.: Absorption and Scattering of Light by Small Particles, John Wiley & Sons, Inc., New York, ISBN-13: 9780471057727, 1983.

Chen, F. and Dudhia, J.: Coupling an Advanced Land Surface–Hydrology Model with the Penn State–NCAR MM5 Modeling System. Part I: Model Implementation and Sensitivity, Mon. Wea. Rev., 129(4), 569–585, doi:10.1175/1520-0493(2001)129<0569:CAALSH>2.0.CO;2, 2001a.

Chen, F. and Dudhia, J.: Coupling an Advanced Land Surface–Hydrology Model with the Penn State–NCAR MM5 Modeling System. Part II: Preliminary Model Validation, Mon. Wea. Rev., 129(4), 587–604, doi:10.1175/1520-0493(2001)129<0587:CAALSH>2.0.CO;2, 2001b.

Derbyshire, E.: Natural Minerogenic Dust and Human Health, AMBIO: A Journal of the Human Environment, 36(1), 73–77, doi:10.1579/0044-7447(2007)36[73:NMDAHH]2.0.CO;2, 2007.

436 Duncan Fairlie, T., Jacob, D. J. and Park, R. J.: The impact of transpacific transport of mineral dust in the
437 United States, Atmospheric Environment, 41(6), 1251–1266, doi:10.1016/j.atmosenv.2006.09.048, 2007.

438 Edgell, H. S.: Arabian Deserts: Nature, Origin and Evolution, Springer Netherlands. [online] Available
439 from: //www.springer.com/gp/book/9781402039690 (Accessed 18 May 2018), 2006.

440 Engelmann, R., Kanitz, T., Baars, H., Heese, B., Althausen, D., Skupin, A., Wandinger, U., Komppula, M.,
441 Stachlewska, I. S., Amiridis, V., Marinou, E., Mattis, I., Linné, H. and Ansmann, A.: The automated
442 multiwavelength Raman polarization and water-vapor lidar PollyXT: the neXT generation, Atmos. Meas.
443 Tech., 9(4), 1767–1784, doi:10.5194/amt-9-1767-2016, 2016.

444 Gerasopoulos, E., Kouvarakis, G., Babasakalis, P., Vrekoussis, M., Putaud, J. and Mihalopoulos, N.: Origin
445 and variability of particulate matter (PM10) mass concentrations over the Eastern Mediterranean,
446 Atmospheric Environment, 40(25), 4679–4690, doi:10.1016/j.atmosenv.2006.04.020, 2006.

447 Gkikas A., Houssos E. E., Lolis C. J., Bartzokas A., Mihalopoulos N. and Hatzianastassiou N.: Atmospheric
448 circulation evolution related to desert-dust episodes over the Mediterranean, Quarterly Journal of the
449 Royal Meteorological Society, 141(690), 1634–1645, doi:10.1002/qj.2466, 2014.

450 Gkikas, A., Obiso, V., Pérez García-Pando, C., Jorba, O., Hatzianastassiou, N., Vendrell, L., Basart, S.,
451 Gassó, S. and Baldasano, J. M.: Direct radiative effects of intense Mediterranean desert dust outbreaks,
452 Atmos. Chem. Phys. Discuss., 2017, 1–67, doi:10.5194/acp-2017-932, 2017.

453 Holben, B. N., Eck, T. F., Slutsker, I., Tanré, D., Buis, J. P., Setzer, A., Vermote, E., Reagan, J. A., Kaufman,
454 Y. J., Nakajima, T., Lavenu, F., Jankowiak, I. and Smirnov, A.: AERONET - A federated instrument network
455 and data archive for aerosol characterization, REMOTE SENS ENVIRON, Remote Sensing & Environment,
456 Remote Sensing Environ, Remote Sensing for Environment, Remote Sensing of Envionment, Remote
457 Sensing of Enviroment, Remote Sensing of environment, Remote Sensing of Environmnt, 66(1), 1–16,
458 doi:10.1016/S0034-4257(98)00031-5, 1998.

459 Hsu, N. C., Tsay, S.-C., King, M. D. and Herman, J. R.: Aerosol properties over bright-reflecting source
460 regions, IEEE Transactions on Geoscience and Remote Sensing, 42(3), 557–569,
461 doi:10.1109/TGRS.2004.824067, 2004.

462 Hsu, N. C., Jeong, M.-J., Bettenhausen, C., Sayer, A. M., Hansell, R., Seftor, C. S., Huang, J. and Tsay, S.-C.:
463 Enhanced Deep Blue aerosol retrieval algorithm: The second generation: ENHANCED DEEP BLUE
464 AEROSOL RETRIEVAL, Journal of Geophysical Research: Atmospheres, 118(16), 9296–9315,
465 doi:10.1002/jgrd.50712, 2013.

466 Iacono Michael J., Delamere Jennifer S., Mlawer Eli J., Shephard Mark W., Clough Shepard A. and Collins
467 William D.: Radiative forcing by long-lived greenhouse gases: Calculations with the AER radiative transfer
468 models, Journal of Geophysical Research: Atmospheres, 113(D13), doi:10.1029/2008JD009944, 2008.

469 Jickells, T. D., An, Z. S., Andersen, K. K., Baker, A. R., Bergametti, G., Brooks, N., Cao, J. J., Boyd, P. W.,
470 Duce, R. A., Hunter, K. A., Kawahata, H., Kubilay, N., laRoche, J., Liss, P. S., Mahowald, N., Prospero, J. M.,

Ridgwell, A. J., Tegen, I. and Torres, R.: Global iron connections between desert dust, ocean biogeochemistry, and climate, Science, 308(5718), 67–71, doi:10.1126/science.1105959, 2005.

Jones, S. L., Adams-Selin, R., Hunt, E. D., Creighton, G. A. and Cetola, J. D.: Update on modifications to WRF-CHEM GOCART for fine-scale dust forecasting at AFWA, AGU Fall Meeting Abstracts, 33, A33D-0188, 2012.

Kaufman Y. J., D. Tanrfi, H. R. Gordon, T. Nakajima, J. Lenoble, R. Frouin, H. Grassl, B. M. Herman, M.D. King, and P.M. Teillet, Passive remote sensing of tropospheric aerosol and atmospheric correction for the aerosol effect, Journal of Geophysical Research: Atmospheres, 102(D14), 16815–16830, doi:10.1029/97JD01496, 1997.

Kalivitis, N., Gerasopoulos, E., Vrekoussis, M., Kouvarakis, G., Kubilay, N., Hatzianastassiou, N., Vardavas, I. and Mihalopoulos, N.: Dust transport over the eastern Mediterranean derived from Total Ozone Mapping Spectrometer, Aerosol Robotic Network, and surface measurements, Journal of Geophysical Research, 112(D3), doi:10.1029/2006JD007510, 2007.

Kallos G., S. Solomos, J. Kushta, C. Mitsakou, C. Spyrou, N. Bartsotas, C Kalogeri: "Natural and Anthropogenic Aerosols in the Mediterranean region and Middle East: Patterns and Impacts", Science of the Total Environment, 2014

Kandler, K., Benker, N., Bundke, U., Cuevas, E., Ebert, M., Knippertz, P., Rodriguez, S., Schuetz, L. and Weinbruch, S.: Chemical composition and complex refractive index of Saharan Mineral Dust at Izana, Tenerife (Spain) derived by electron microscopy, Atmos. Environ., 41(37), 8058–8074, doi:10.1016/j.atmosenv.2007.06.047, 2007.

Kaplan Michael L., Vellore Ramesh K., Lewis John M., Underwood S. Jeffrey, Pauley Patricia M., Martin Jonathan E., Rabin Robert M. and Krishnan R.: Subtropical-polar jet interactions in Southern Plains dust storms, Journal of Geophysical Research: Atmospheres, 118(23), 12,893-12,914, doi:10.1002/2013JD020345, 2013.

Kosmopoulos Panagiotis G., Stelios Kazadzis, Michael Taylor, Eleni Athanasopoulou, Orestis Speyer, Panagiotis I. Raptis, Eleni Marinou, Emmanouil Proestakis, Stavros Solomos, Evangelos Gerasopoulos, Vassilis Amiridis, Alkiviadis Bais, and Charalabos Kontoes, Atmos. Meas. Tech., 10, 2435-2453, https://doi.org/10.5194/amt-10-2435-2017, 2017

Koulouri, E., Saarikoski, S., Theodosi, C., Markaki, Z., Gerasopoulos, E., Kouvarakis, G., Mäkelä, T., Hillamo, R. and Mihalopoulos, N.: Chemical composition and sources of fine and coarse aerosol particles in the Eastern Mediterranean, Atmospheric Environment, 42(26), 6542–6550, doi:10.1016/j.atmosenv.2008.04.010, 2008.

Kouroutzoglou, J., Flocas, H. A., Hatzaki, M., Keay, K., Simmonds, I. and Mavroudis, A.: On the dynamics of a case study of explosive cyclogenesis in the Mediterranean, Meteorol. Atmos. Phys., 127(1), 49–73, doi:10.1007/s00703-014-0357-x, 2015.

506 Kushta J., Kallos G., Astitha M., Solomos S., Spyrou C., Mitsakou C. and Lelieveld J.: Impact of natural
507 aerosols on atmospheric radiation and consequent feedbacks with the meteorological and
508 photochemical state of the atmosphere, Journal of Geophysical Research: Atmospheres, 119(3), 1463–
509 1491, doi:10.1002/2013JD020714, 2013.

510 Lelieveld, J., Berresheim, H., Borrmann, S., Crutzen, P. J., Dentener, F. J., Fischer, H., Feichter, J., Flatau,
511 P. J., Heland, J., Holzinger, R., Korrmann, R., Lawrence, M. G., Levin, Z., Markowicz, K. M., Mihalopoulos,
512 N., Minikin, A., Ramanathan, V., de Reus, M., Roelofs, G. J., Scheeren, H. A., Sciare, J., Schlager, H.,
513 Schultz, M., Siegmund, P., Steil, B., Stephanou, E. G., Stier, P., Traub, M., Warneke, C., Williams, J. and
514 Ziereis, H.: Global air pollution crossroads over the Mediterranean, Science, 298(5594), 794–799,
515 doi:10.1126/science.1075457, 2002.

516 Levy, R. C., Remer, L. A., Kleidman, R. G., Mattoo, S., Ichoku, C., Kahn, R. and Eck, T. F.: Global evaluation
517 of the Collection 5 MODIS dark-target aerosol products over land, Atmos. Chem. Phys., 10(21), 10399–
518 10420, doi:10.5194/acp-10-10399-2010, 2010.

519 Levy, R. C., Mattoo, S., Munchak, L. A., Remer, L. A., Sayer, A. M., Patadia, F. and Hsu, N. C.: The
520 Collection 6 MODIS aerosol products over land and ocean, Atmos. Meas. Tech., 6(11), 2989–3034,
521 doi:10.5194/amt-6-2989-2013, 2013.

522 Mamouri, R.-E., Ansmann, A., Nisantzi, A., Solomos, S., Kallos, G. and Hadjimitsis, D. G.: Extreme dust
523 storm over the eastern Mediterranean in September 2015: satellite, lidar, and surface observations in
524 the Cyprus region, Atmos. Chem. Phys., 16(21), 13711–13724, doi:10.5194/acp-16-13711-2016, 2016.

525 Marticorena, B. and Bergametti, G.: Modeling the atmospheric dust cycle: 1. Design of a soil derived
526 dust emission scheme, J. Geophys. Res., 100(D8), 16415–16430, Atmospheres, 100(D8), 16415–16430,
527 doi:10.1029/95JD00690, 1995.

528 Marinou, E., Amiridis, V., Binietoglou, I., Tsikerdekis, A., Solomos, S., Proestakis, E., Konsta, D.,
529 Papagiannopoulos, N., Tsekeri, A., Vlastou, G., Zanis, P., Balis, D., Wandinger, U. and Ansmann, A.: Three-
530 dimensional evolution of Saharan dust transport towards Europe based on a 9-year EARLINET-optimized
531 CALIPSO dataset, Atmos. Chem. Phys., 17(9), 5893–5919, doi:10.5194/acp-17-5893-2017, 2017.

532 Mie, G.: Beiträge zur Optik trüber Medien, speziell kolloidaler Metallösungen, Ann. Phys.-Berlin, Vierte
533 Folge, 25, 77–445, 1908.

534 Mitsakou, C., Kallos, G., Papantoniou, N., Spyrou, C., Solomos, S., Astitha, M. and Housiadas, C.: Saharan
535 dust levels in Greece and received inhalation doses, Atmos. Chem. Phys., 8(23), 7181–7192,
536 doi:10.5194/acp-8-7181-2008, 2008.

537 Nastos, P. T., Paliatsos, A. G., Anthracopoulos, M. B., Roma, E. S., Priftis, K. N.: Outdoor particulate
538 matter and childhood asthma admissions in Athens, Greece: a time-series study, Environ. Health, 9:45,
539 http://www.ehjournal.net/content/9/1/45, 2010.

Nastos, P. T., Kampanis, N. A., Giaouzaki, K. N. and Matzarakis, A.: Environmental impacts on human health during a Saharan dust episode at Crete Island, Greece, Meteorologische Zeitschrift, 517–529, doi:10.1127/0941-2948/2011/0246, 2011.

Nastos, P. T.: Meteorological Patterns Associated with Intense Saharan Dust Outbreaks over Greece in Winter, Advances in Meteorology, doi:10.1155/2012/828301, 2012.

Nastos, Bleta, A. G. and Matsangouras, I. T.: Human thermal perception related to Föhn winds due to Saharan dust outbreaks in Crete Island, Greece, Theoretical and Applied Climatology, 128, 635–647, doi:10.1007/s00704-015-1724-3, 2017.

Okin, G., Parsons, A., Wainwright, J., Herrick, J., Bestelmeyer, B., Peters, D. and Fredrickson, E.: Do Changes in Connectivity Explain Desertification?, Bioscience, 237–244, 2009.

Papayannis, A., Mamouri, R. E., Amiridis, V., Kazadzis, S., Pérez, C., Tsaknakis, G., Kokkalis, P. and Baldasano, J. M.: Systematic lidar observations of Saharan dust layers over Athens, Greece in the frame of EARLINET project (2004–2006), Ann. Geophys., 27(9), 3611–3620, doi:10.5194/angeo-27-3611-2009, 2009.

Pielke, R. A. S., 2002: Mesoscale Meteorological Modeling. 2nd ed. International Geophysics Series, Vol. 78, Academic Press, 676 pp., 2002.

Pytharoulis I., Analysis of a Mediterranean tropical-like cyclone and its sensitivity to the sea surface temperatures, Atmospheric Research, DOI: 10.1016/j.atmosres.2017.08.009, 2017

Remer, L. A., Kaufman, Y. J., Tanré, D., Mattoo, S., Chu, D. A., Martins, J. V., Li, R.-R., Ichoku, C., Levy, R. C., Kleidman, R. G., Eck, T. F., Vermote, E. and Holben, B. N.: The MODIS Aerosol Algorithm, Products, and Validation, J. Atmos. Sci., 62(4), 947–973, doi:10.1175/JAS3385.1, 2005.

Remer, L. A., Kleidman, R. G., Levy, R. C., Kaufman, Y. J., Tanre, D., Mattoo, S., Martins, J. V., Ichoku, C., Koren, I., Yu, H. and Holben, B. N.: Global aerosol climatology from the MODIS satellite sensors, J. Geophys. Res.-Atmos., 113(D14), D14S07, doi:10.1029/2007JD009661, 2008.

Samoli, E., Nastos, P. T., Paliatsos, A. G., Katsouyanni, K. and Priftis, K. N.: Acute effects of air pollution on pediatric asthma exacerbation: evidence of association and effect modification, Environ. Res., 111(3), 418–424, doi:10.1016/j.envres.2011.01.014, 2011.

Sayer, A. M., Hsu, N. C., Bettenhausen, C. and Jeong, M.-J.: Validation and uncertainty estimates for MODIS Collection 6 “Deep Blue” aerosol data, J. Geophys. Res.-Atmos., 118(14), 7864–7872, doi:10.1002/jgrd.50600, 2013.

Sayer, A. M., Munchak, L. A., Hsu, N. C., Levy, R. C., Bettenhausen, C. and Jeong, M.-J.: MODIS Collection 6 aerosol products: Comparison between Aqua’s e-Deep Blue, Dark Target, and “merged” data sets, and usage recommendations, J. Geophys. Res.-Atmos., 119(24), 13965–13989, doi:10.1002/2014JD022453, 2014.

574 Schepanski K., Knippertz P., Fiedler S., Timouk F. and Demarty J.: The sensitivity of nocturnal low-level
575 jets and near-surface winds over the Sahel to model resolution, initial conditions and boundary-layer
576 set-up, Quarterly Journal of the Royal Meteorological Society, 141(689), 1442–1456,
577 doi:10.1002/qj.2453, 2014.

578 Solomos, S., Kallos, G., Kushta, J., Astitha, M., Tremback, C., Nenes, A. and Levin, Z.: An integrated
579 modeling study on the effects of mineral dust and sea salt particles on clouds and precipitation, Atmos.
580 Chem. Phys., 11(2), 873–892, doi:10.5194/acp-11-873-2011, 2011.

581 Solomos, S., Kallos, G., Mavromatidis, E. and Kushta, J.: Density currents as a desert dust mobilization
582 mechanism, Atmos. Chem. Phys., 12(22), 11199–11211, doi:10.5194/acp-12-11199-2012, 2012.

583 Solomos, S., Ansmann, A., Mamouri, R.-E., Binietoglou, I., Patlakas, P., Marinou, E. and Amiridis, V.:
584 Remote sensing and modelling analysis of the extreme dust storm hitting the Middle East and eastern
585 Mediterranean in September 2015, Atmos. Chem. Phys., 17(6), 4063–4079, doi:10.5194/acp-17-4063-
586 2017, 2017.

587 Spyrou C., Direct radiative impacts of desert dust on atmospheric water content, Aerosol Science and
588 Technology, 52:6, 693-701, DOI: 10.1080/02786826.2018.1449940, 2018

589 Su Lin and Fung Jimmy C. H.: Sensitivities of WRF-Chem to dust emission schemes and land surface
590 properties in simulating dust cycles during springtime over East Asia, Journal of Geophysical Research:
591 Atmospheres, 120(21), 11,215-11,230, doi:10.1002/2015JD023446, 2015.

592 Tanre, D., Kaufman, Y. J., Herman, M. and Mattoo, S.: Remote sensing of aerosol properties over oceans
593 using the MODIS/EOS spectral radiances, J. Geophys. Res.-Atmos., 102(D14), 16971–16988,
594 doi:10.1029/96JD03437, 1997.

595 Wesely, M.: Parameterization of Surface Resistances to Gaseous Dry Deposition in Regional-Scale
596 Numerical-Models, Atmos. Environ., 23(6), 1293–1304, doi:10.1016/0004-6981(89)90153-4, 1989.

597 Zender, C. S., Bian, H. S. and Newman, D.: Mineral Dust Entrainment and Deposition (DEAD) model:
598 Description and 1990s dust climatology, J. Geophys. Res.-Atmos., 108(D14), 4416,
599 doi:10.1029/2002JD002775, 2003.

600

601

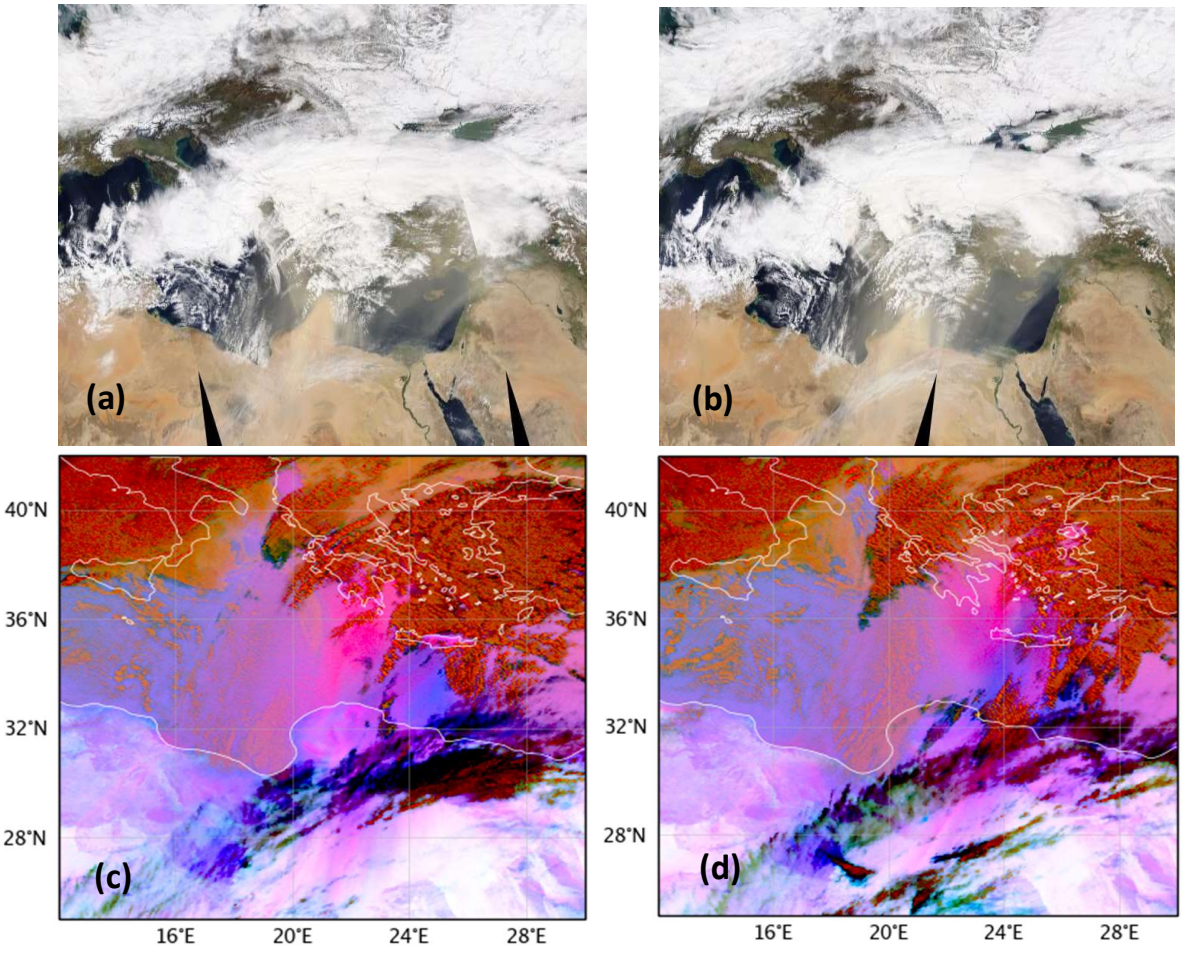

602

603 Figure 1. Up(a,b): True color images from MODIS-Terra (left) and MODIS-Aqua (right) on 22nd March
604 2018. Down (c,d): MSG-SEVIRI dust RGB images on 12:00 UTC (left) and 15:00 UTC (right), 22 March
605 2018.

606

607

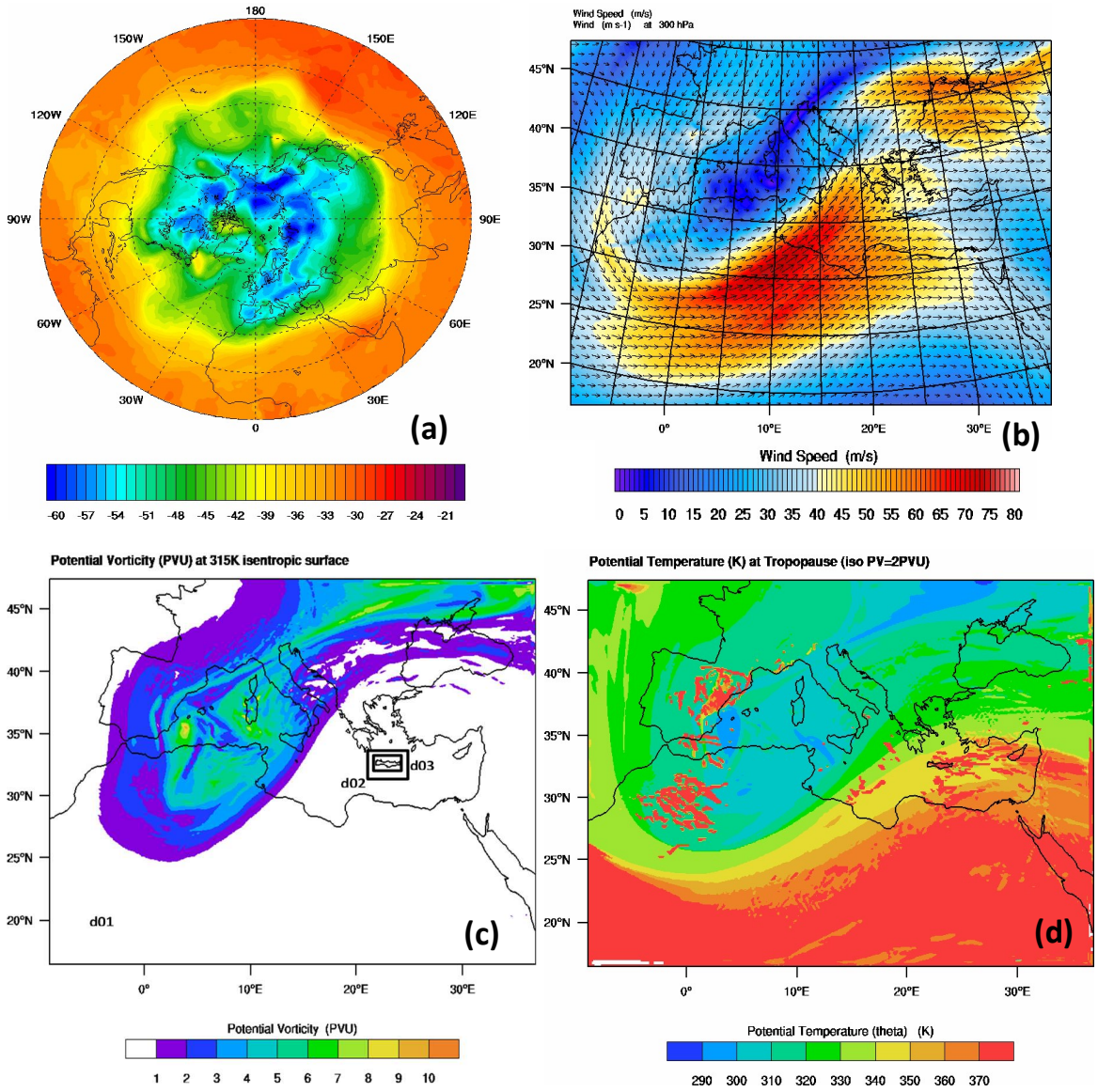

608

609

610 Figure 2. a) Temperature at 300 hPa, 21 March 2018, 12:00 UTC b) Wind speed and vectors at 300 hPa,
611 22 March 06:00 UTC c) Potential Vorticity (PVU) at the 315K isentropic surface, 22 March 06:00 UTC and
612 the three domain structure (d01,d02,d03), d) Potential temperature (K) at 2PVU iso-PV surface, 22
613 March 06:00 UTC

Preprints (www.preprints.org) | NOT PEER-REVIEWED | Posted: 23 May 2018 doi:10.20944/preprints201805.0321.v1

Peer-reviewed version available at Atmosphere 2018, 9, 240; doi:10.3390/atmos9070240

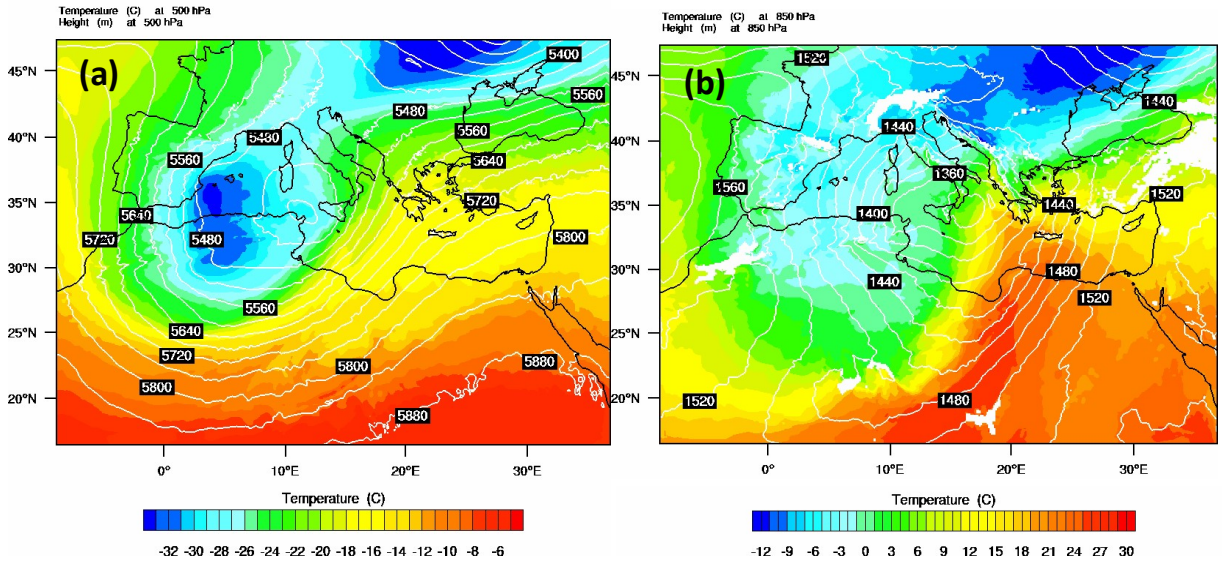

614

615 Figure 3. a) Temperature (°C) and geopotential height (white contours every 40 m) at 500 hPa and b)
616 Temperature (°C) and geopotential height (white contours every 20 m) at 850 hPa, 22 March 2018,
617 06:00 UTC.

618

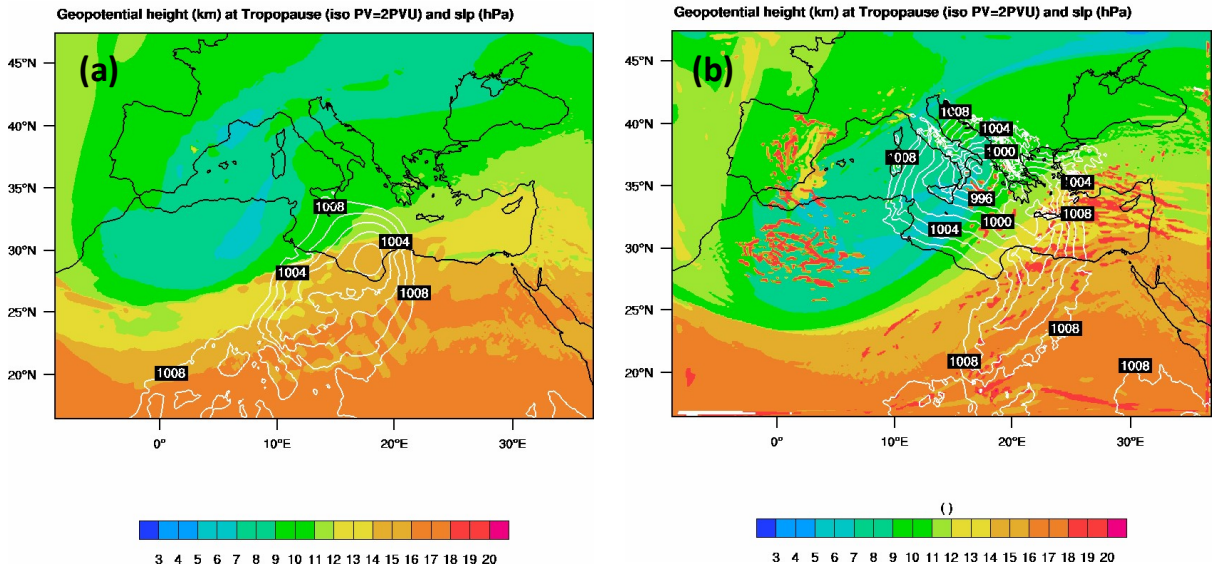

619

620 Figure 4. Geopotential height (km) at the dynamical tropopause (iso-PV=2PVU) and sea level pressure
621 (white contours every 2 hPa) at: a) 21 March 2018, 18:00 UTC and b) 22 March 2018, 12:00 UTC

622

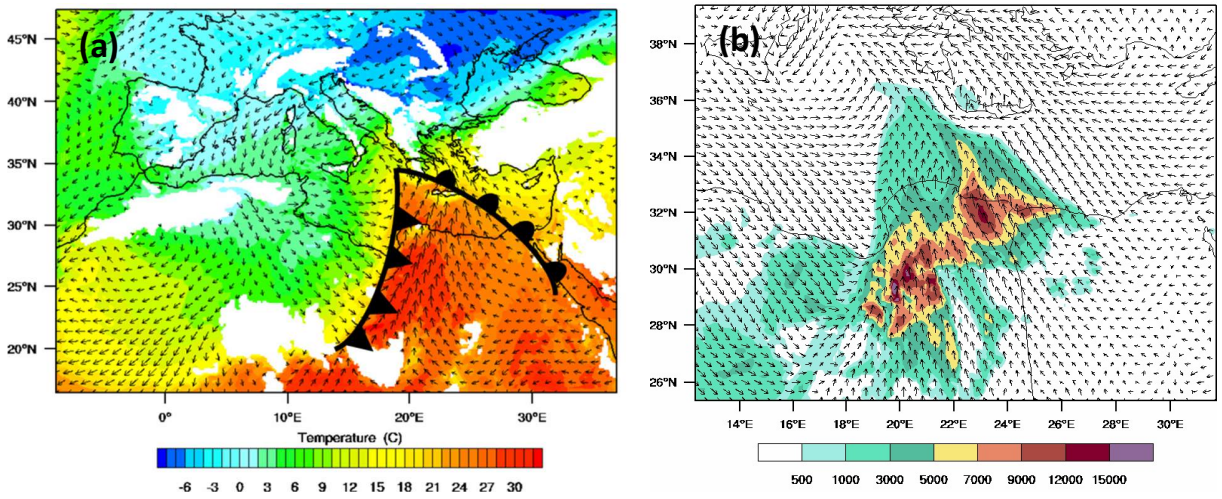

623

624 Figure 5. a) Frontal activity, temperature (°C) and wind vectors at 925 hPa and b) Near surface dust
625 concentration (μg m^{-3}) and wind vectors at 10m (zoom from the external 12×12 km domain), on 22
626 March 2018 06:00 UTC

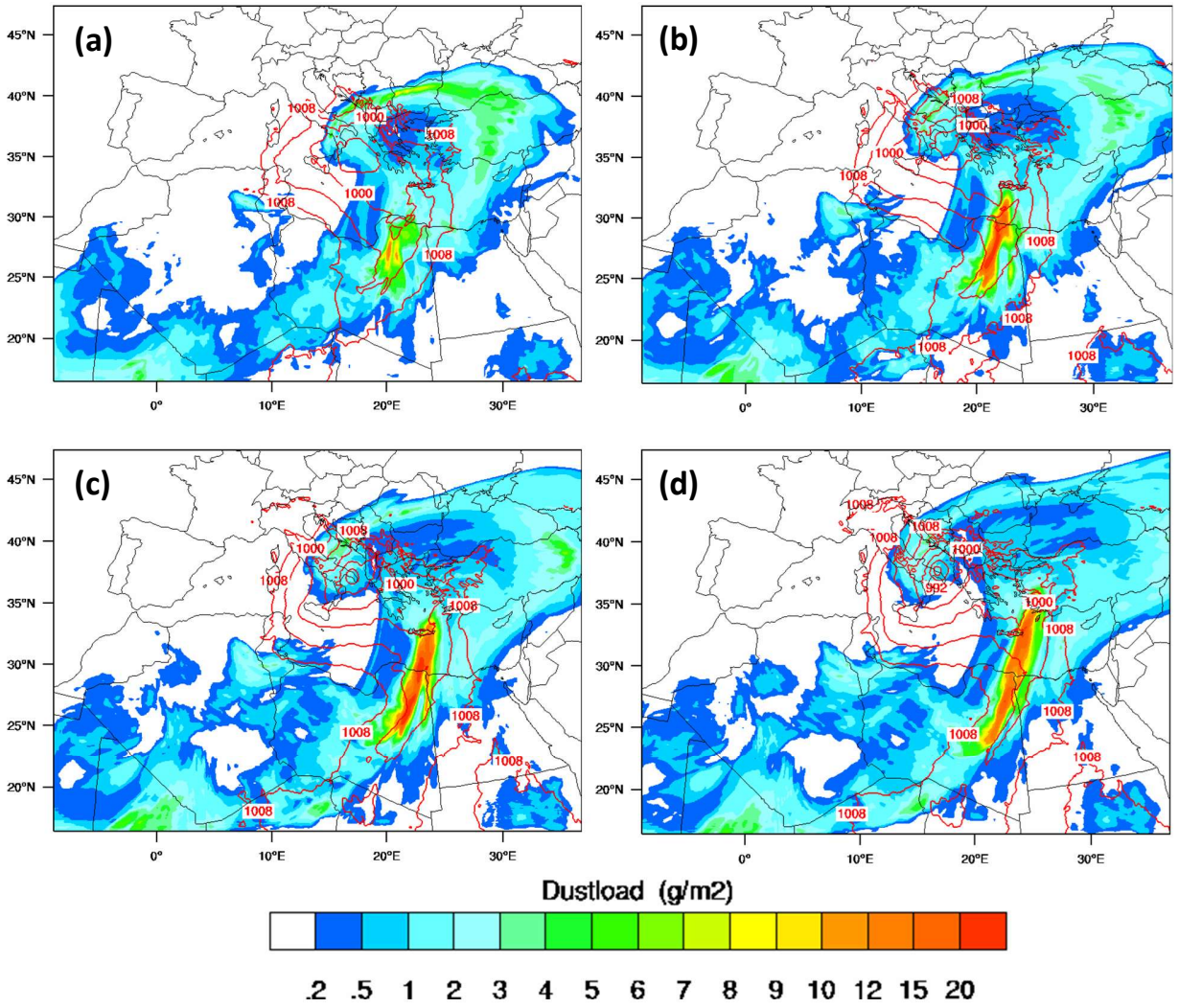

627

628 Figure 6. Dustload (mg m^{-2}) and slp (red contours every 4 hPa) on 22 March 2018: a) 09:00 UTC; b) 12:00
629 UTC; c) 15:00 UTC; d) 18:00 UTC (dust transport along the warm conveyor belt)

630

631

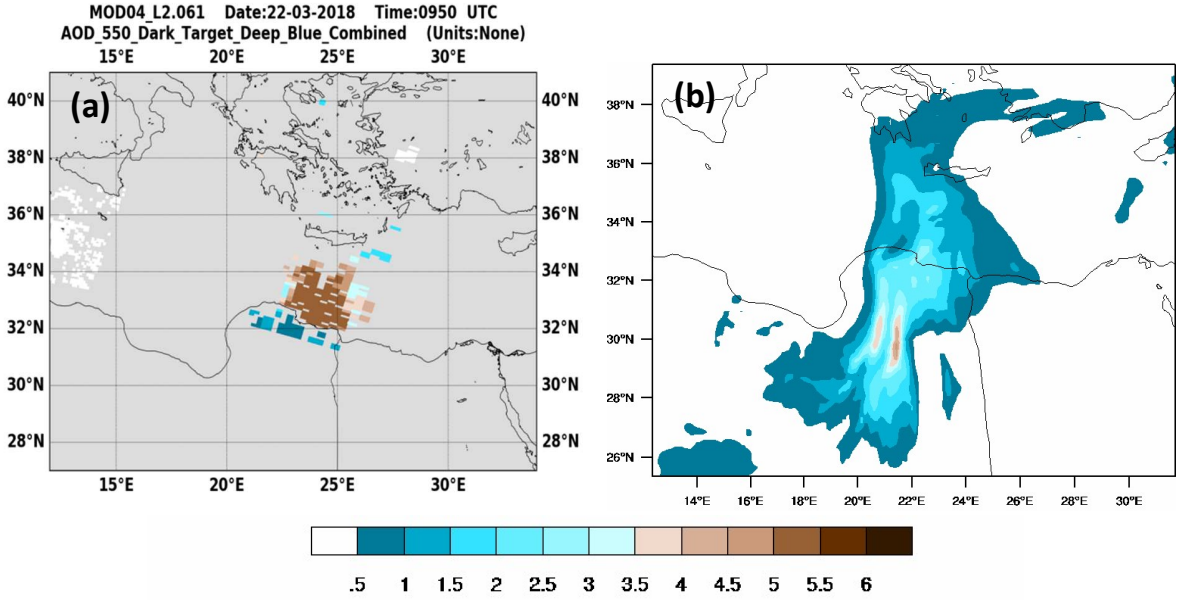

632

633 Figure 7. a) MODIS AOD at 09:50 UTC; b) WRF-Chem AOD at 10:00 UTC, 22 March 2018

634

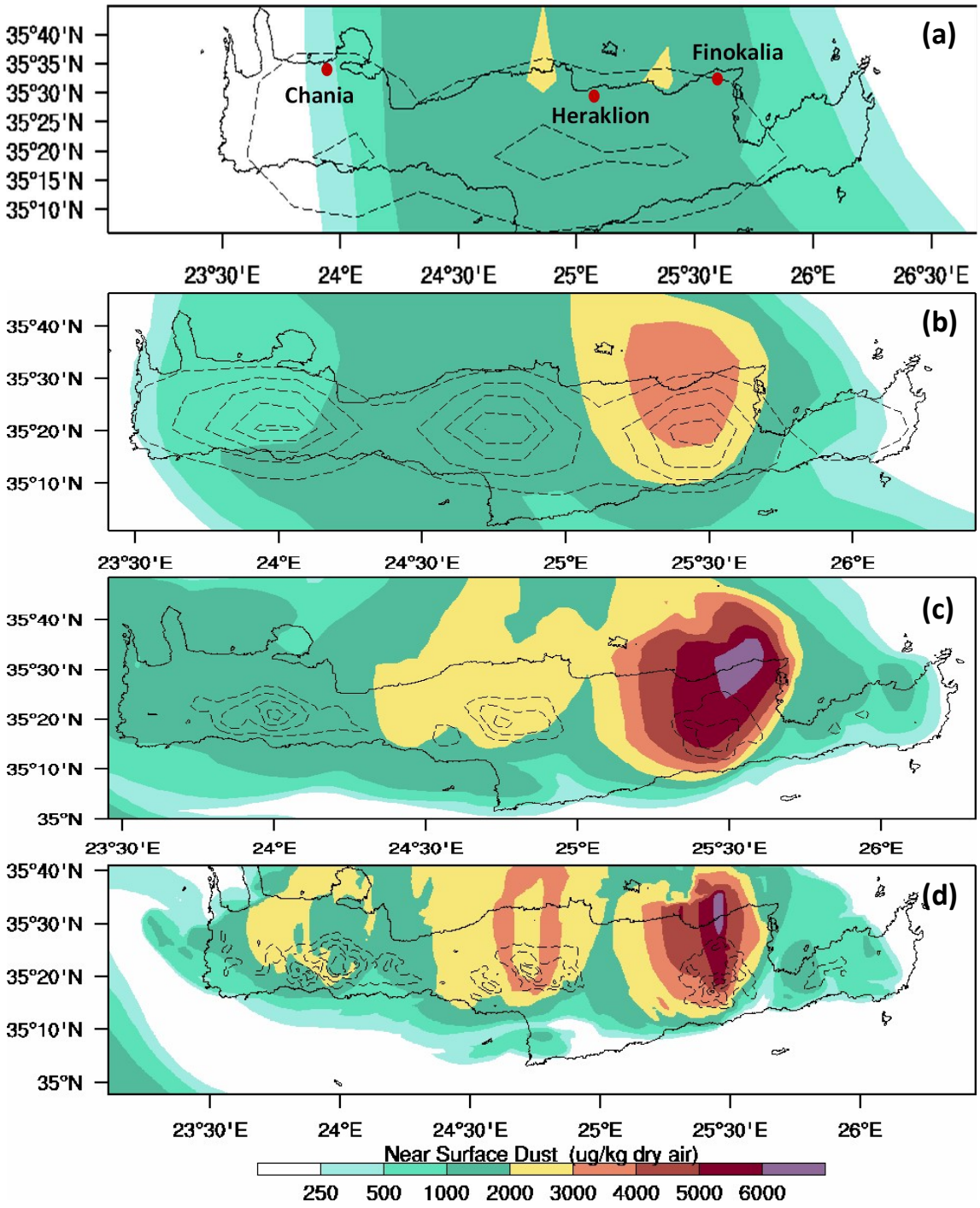

Figure 8. Surface dust concentration (μg m^{-3}) and topographic contours on 22 March 2018, 15:00 UTC a) 24×24 km grid-space, topography from 200m to 1000 m by 200 m; b) 12×12 km grid-space, topography from 200m to 1000 m by 200 m; c) 3×3 km grid-space, topography from 750m to 2000 m by 500 m; d) 1×1 km grid-space, topography from 750m to 2000 m by 500 m

Preprints (www.preprints.org) | NOT PEER-REVIEWED | Posted: 23 May 2018 doi:10.20944/preprints201805.0321.v1

Peer-reviewed version available at Atmosphere 2018, 9, 240; doi:10.3390/atmos9070240

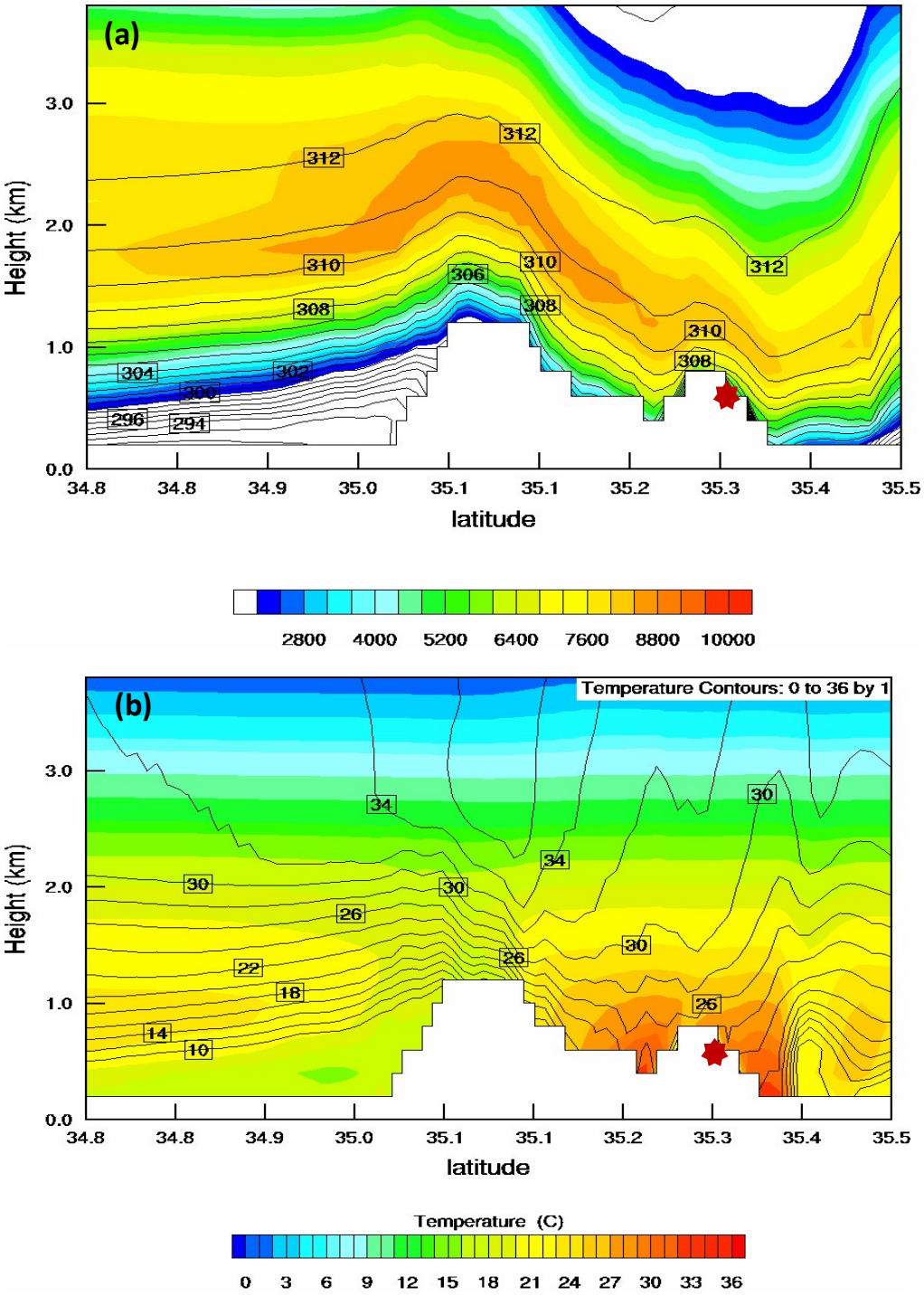

Figure 9. Model cross-section over Finokalia from the inner 1×1 km grid at 16:00 UTC, 22 March 2018: a) Dust concentration (color scale in μg m^{-3}) and potential temperature (line contours) and b) temperature (color scale in °C) and wind speed (line contours every 2 m s^{-1}) at 17:00 UTC, 22 March 2018. The red start roughly depicts the location of Finokalia station.

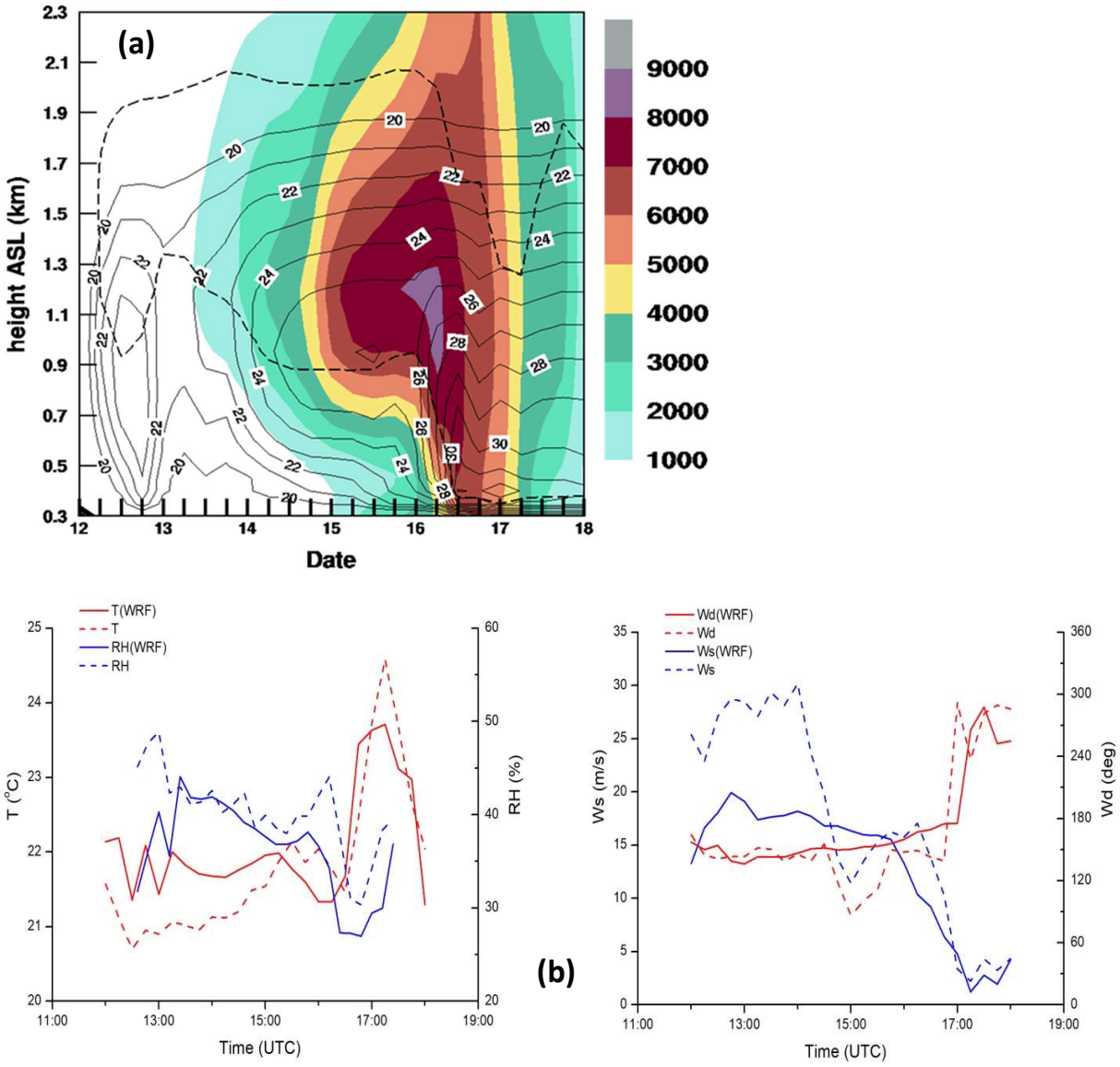

Figure 10. a) Time-height cross section over Finokalia every 15 minutes from the 1×1 km domain, during 12:00-18:00 UTC, 22 March 2018. The color scale represents dust concentration (μg m^{-3}), black line contours is the ambient temperature (°C) and the dashed line represents 10% relative humidity. b) Measured and modeled temperature (°C), wind speed (m s^{-1}), wind direction (degrees) and relative humidity (%) at the station of Finokalia, 12:00-18:00 UTC, 22 March 2018.

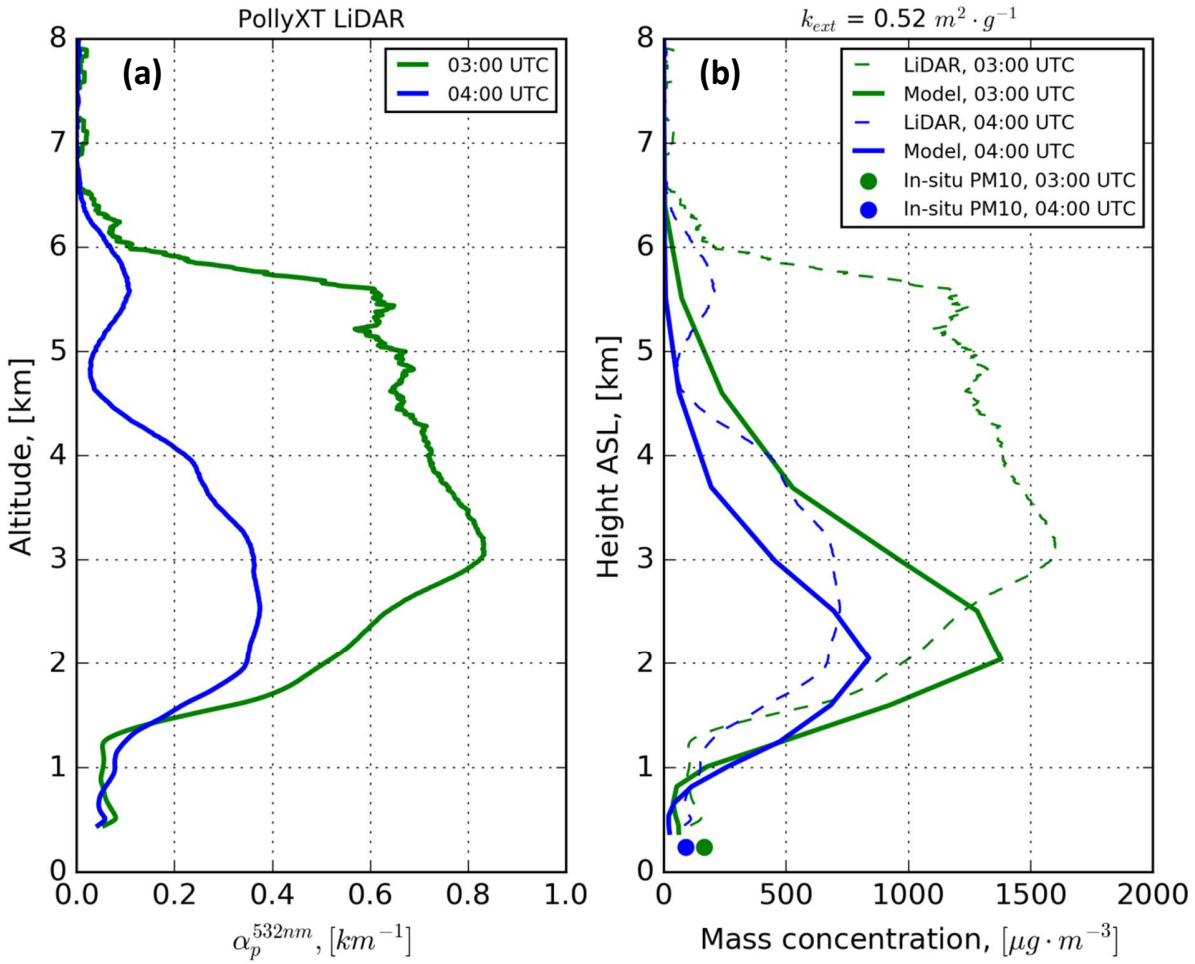

Figure 11. a) PollyXT LiDAR particle extinction coefficient profiles (\alpha_{p}^{532nm}) at 532nm for 03:00 and 04:00 UTC (green and blue line respectively). The colored dots represent the corresponding in-situ PM10 measurements.

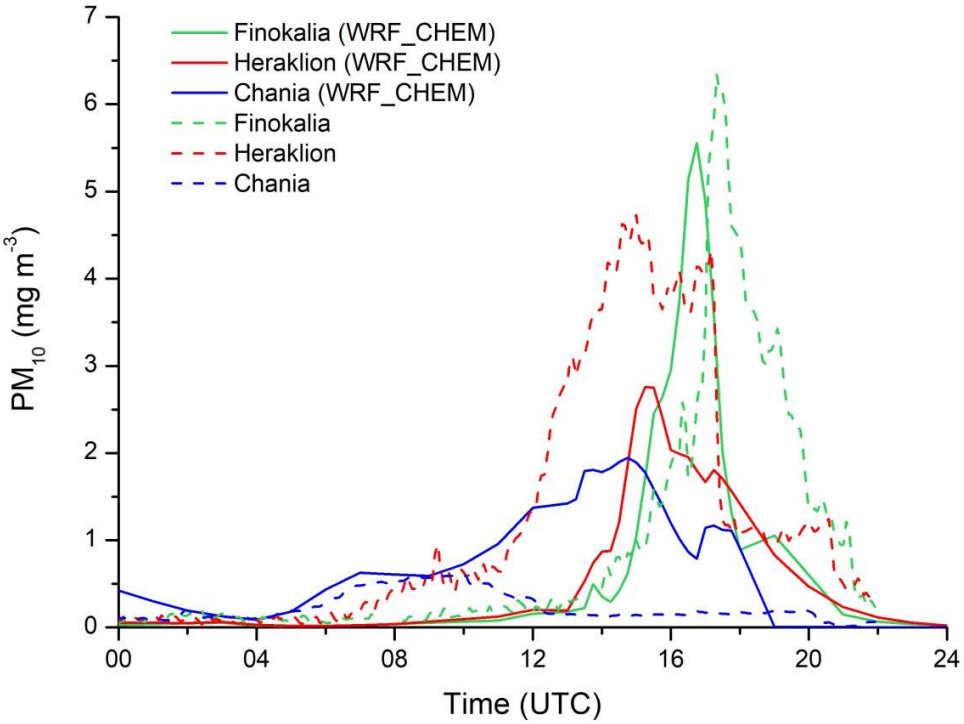

662

663 Figure 12. Timeseries of observed (dashed lines) and modeled (solid lines) PM10 at Finokalia,
664 Heraklion and Chania on 22 March 2018.

665